Two-photon frequency division multiplexing for functional *in vivo* imaging: a feasibility study.

DMITRI TSYBOULSKI[*], NATALIA ORLOVA, PETER LEDOCHOWITSCH, AND PETER SAGGAU

Allen Institute, 615 Westlake Ave N, Seattle, WA 98109, USA
*dmitrit@alleninstitute.org

Abstract: Recently, we presented a new approach to create high-speed amplitude modulation of femtosecond laser pulses in the MHz range to tag multiple excitation beams and their corresponding fluorescence signals with specific frequencies. In this work, we discuss the sensitivity of this method and its utility for *in vivo* recordings of Ca^{2+} signals in brain tissue compared to conventional two-photon laser scanning microscopy. While frequency-multiplexed imaging appears slightly inferior in terms of image quality due to shot noise-induced cross-talk between individual frequency channels, the specific application of the technique for recording average signals from selected regions of interest such as neuronal cell bodies is found to be exceptionally promising. We used phase information contained within each pixel of the selected area represented by a short waveform to phase-align and recombine them into one extended waveform, thereby effectively increasing the waveform measurement time. This procedure narrows the detection band of a digital lock-in filter and thus decreases noise contributions from other frequency channels by more than an order of magnitude.

References and Links

1. W. Denk, J. H. Strickler, and W. W. Webb, "Two-photon laser scanning fluorescence microscopy," Science **248**, 73-76 (1990).
2. N. Ji, J. Freeman, and S. L. Smith, "Technologies for imaging neural activity in large volumes," Nat. Neurosci. **19**, 1154-1164 (2016).
3. N. J. Sofroniew, D. Flickinger, J. King, and K. Svoboda, "A large field of view two-photon mesoscope with subcellular resolution for in vivo imaging," eLife **5**, e14472-1-20 (2016).
4. W. Yang, and R. Yuste, "In vivo imaging of neural activity," Nat. Methods **14**, 349-359 (2017).
5. L. Kong, J. Tang, J. P. Little, Y. Yu, T. Lammermann, C. P. Lin, R. N. Germain, and M. Cui, "Continuous volumetric imaging via an optical phase-locked ultrasound lens," Nat. Methods **12**, 759-762 (2015).
6. R. Lu, W. Sun, Y. Liang, A. Kerlin, J. Bierfeld, J. D. Seelig, D. E. Wilson, B. Scholl, B. Mohar, M. Tanimoto, M. Koyama, D. Fitzpatrick, M. B. Orger, and N. Ji, "Video-rate volumetric functional imaging of the brain at synaptic resolution," Nat. Neurosci. **20**, 620-628 (2017).
7. R. Prevedel, A. J. Verhoef, A. Pernia-Andrade, S. Weisenburger, B. S. Huang, T. Nobauer, A. Fernandez, J. E. Delcour, P. Golshani, A. Baltuska, and A. Vaziri, "Fast volumetric calcium imaging across multiple cortical layers using sculpted light," Nat. Methods **14**, 1021–1028 (2016).
8. Song, A. S. Charles, S. A. Koay, J. L. Gauthier, S. Y. Thiberge, J. W. Pillow, and D. W. Tank, "Volumetric two-photon imaging of neurons using stereoscopy (VTWINS)," Nat. Methods **14**, 420–426 (2017).
9. G. D. Reddy, K. Kelleher, R. Fink, and P. Saggau, "Three-dimensional random access multiphoton microscopy for functional imaging of neuronal activity," Nat. Neurosci. **11**, 713-720 (2008).
10. K. P. Lillis, A. Eng, J. A. White, and J. Mertz, "Two-photon imaging of spatially extended neuronal network dynamics with high temporal resolution," J. Neurosci. Methods **172**, 178-184 (2008).
11. G. Katona, G. Szalay, P. Maak, A. Kaszas, M. Veress, D. Hillier, B. Chiovini, E. S. Vizi, B. Roska, and B. Rozsa, "Fast two-photon in vivo imaging with three-dimensional random-access scanning in large tissue volumes," Nat. Methods **9**, 201-208 (2012).
12. J. N. Stirman, I. T. Smith, M. W. Kudenov, and S. L. Smith, "Wide field-of-view, multi-region, two-photon imaging of neuronal activity in the mammalian brain," Nat. Biotechnol. **34**, 857-862 (2016).
13. Cheng, J. T. Goncalves, P. Golshani, K. Arisaka, and C. Portera-Cailliau, "Simultaneous two-photon calcium imaging at different depths with spatiotemporal multiplexing," Nat. Methods **8**, 139-142 (2011).
14. M. Ducros, H. Y. Goulam, J. Bradley, S. de, V, and S. Charpak, "Encoded multisite two-photon microscopy," Proc. Natl. Acad. Sci. U.S.A. **110**, 13138-13143 (2013).
15. S. S. Howard, A. Straub, N. G. Horton, D. Kobat, and C. Xu, "Frequency-multiplexed in vivo multiphoton phosphorescence lifetime microscopy," Nat. Photon. **7**, 33-37 (2013).

16. J. L. Chen, F. F. Voigt, M. Javadzadeh, R. Krueppel, and F. Helmchen, "Long-range population dynamics of anatomically defined neocortical networks," eLife **5**, e14679-1-26 (2016).
17. D. Tsyboulski, N. Orlova, and P. Saggau, "Amplitude modulation of femtosecond laser pulses in the megahertz range for frequency-multiplexed two-photon imaging," Opt. Express **25**, 9435-9442 (2017).
18. J. B. Pawley, "Fundamental limits in confocal microscopy," in *Handbook of biological confocal microscopy* (Springer, 2006).
19. J. R. Janesik, *Photon transfer* (SPIE Press, 2007).
20. S. E. Bohndiek, A. Blue, A. T. Clark, M. L. Prydderch, and R. Turchetta, "Comparison of methods for estimating the conversion gain of cmos active pixel sensors," IEEE Sens. J. **8**, 1734 (2008).
21. J. J. Field, K. K. Wersing, S. R. Dominique, A. M. Allende Motz, K. F. DeLuca, D. H. Levi, J. G. DeLuca, M. D. Young, J. A. Squier, and R. A. Bartels, "Superresolved multiphoton microscopy with spatial frequency-modulated imaging," Proc. Natl. Acad. Sci. U.S.A. **113**, 6605-6610 (2016).
22. K. Podgorski, and G. Ranganathan, "Brain heating induced by near-infrared lasers during multiphoton microscopy," J. Neurophysiol. **116**, 1012-1023 (2016).
23. R. Yang, T. D. Weber, E. D. Witkowski, I. G. Davison, and J. Mertz, "Neuronal imaging with ultrahigh dynamic range multiphoton microscopy," Sci. Rep. **7**, 5817-5811-5817 (2017).
24. Podor, Y. Hu, M. Ohkura, J. Nakai, R. Croll, and A. Fine, "Comparison of genetically encoded calcium indicators for monitoring action potentials in mammalian brain by two-photon excitation fluorescence microscopy," Neurophotonics **2**, 021014-1-7 (2015).
25. J. Lecoq, J. Savall, D. Vucinic, B. F. Grewe, H. Kim, J. Z. Li, L. J. Kitch, and M. J. Schnitzer, "Visualizing mammalian brain area interactions by dual-axis two-photon calcium imaging," Nat. Neurosci. **17**, 1825-1829 (2014).

1.   Introduction

Two-photon laser scanning microscopy (TPLSM) [1] has become a standard tool for functional imaging of neural activity with sub-cellular resolution. Conventional TPLSM can achieve maximal data acquisition rates up to 50 frames per second [2, 3], which is sufficient for monitoring Ca^{2+}–associated fluorescence signal transients within one or several imaging planes with satisfactory temporal resolution. Although highly desired, simultaneous functional recordings from large ensembles of neurons labeled with calcium- or voltage-sensitive indicators remain challenging due to limitations in TPLSM scan speeds and data acquisition rates [2, 4]. A variety of experimental techniques have emerged designed to improve the speed of imaging over a larger area or a volume. These can be generally assigned to several broad categories: those increasing the sweep rate at which a focused beam moves through the volume [5], those involving engineered excitation point spread function to increase the individual voxel size in a volume [6-8], and those restricting the imaging volume to selected regions of interest (ROI) [9-11]. For example, several reports demonstrated functional imaging of cell activity within $(0.5 \text{ mm})^3$ at the rate of several Hz [6, 7]. Nevertheless, emergence of new imaging systems with a significantly larger field-of-view (FOV) and more than an order of magnitude increase in the accessible imaging volume [3, 12] again raises the issue of limited data acquisition rates in TPLSM.

To address emerging needs of large FOV systems, a separate class of techniques may be employed. These methods are focused on multiplexed image acquisition, where the sample is scanned with multiple excitation beams and the emission is recorded with a single detector [12-16]. One approach, termed "spatiotemporal multiplexing," utilized multiple excitation pulse trains delayed in time relative to each other and separated the corresponding emission signals based on their arrival time at a detector [12, 13, 16]. The useful number of acquisition channels was ultimately limited by the laser pulse repetition rate and the fluorescence lifetime of the fluorophore, leaving room only for a few multiplexed channels with commonly used commercial 80 MHz femtosecond pulsed lasers.

Recently we introduced a new two-photon frequency-division multiplexing microscopy (TPFDMM) method to create amplitude modulation of femtosecond laser pulses in the MHz range based on interference of periodically phase-shifted femtosecond pulse trains, and demonstrated frequency-multiplexed two-photon imaging in test samples [17]. The major limiting factor of this approach is shot noise, whose average spectral density is distributed uniformly across the detection frequency bandwidth, and, therefore, induces cross-talk between individual frequency channels. While it has been predicted that the signal-to-noise ratios (SNR) in TPFDMM and conventional TPLSM images are similar, given the same data acquisition rate and the same average emission intensity per channel [17], TPFDMM data is contaminated with cross-talk related ghost images from other active channels. At high scanning speeds provided by resonance galvanometer (RG) scanners individual pixel dwell times become less than 100 ns. Together with low emission signal intensities, this may result in unacceptably low contrast between individual frequency channels in TPFDMM. In this work, we analyze the performance of TPFDMM in more detail and demonstrate its utility for recording Ca^{2+} signals *in vivo*. Most importantly, we propose a novel method of incorporating phase information to the analysis of functional signals that leads to more than an order of magnitude reduction in cross-talk between frequency-encoded imaging channels.

2. Methods

High-speed amplitude modulation of multiple excitation beams derived from a single mode-locked Ti:Sapphire laser (Chameleon Ultra II, Coherent) was created by interfering femtosecond laser pulses with a periodic phase shift produced by acousto-optic deflectors (AODs, DTSX-A12-800.1000, AA Opto-electronic) with a custom-built Mach-Zehnder interferometer. In the present work, 3 excitation beams with equal angular offset and modulation frequencies of 1, 5, 7 MHz were generated. Imaging of tissue slices was performed on a custom-built TPLSM system, equipped with XY galvanometer scanners (6240H, Cambridge Technology), and a water immersion objective lens (25× XLPLAN N, Olympus). Emission within a 500-700 nm spectral window was detected by a hybrid avalanche photodetector (R11322U-40, Hamamatsu), connected to a pre-amplifier (DHCPA100, 200 MHz bandwidth, FEMTO), and sampled with a streaming waveform digitizer at 500 MS/s (ATS9350, AlazarTech). Galvo-scanners were controlled with two DAQ boards (PCIe-6353, National Instruments), which also triggered waveform acquisition of each scan line.

Custom MATLAB (MathWorks) routines were used for numerical modeling and analysis of amplitude-modulated emission signals. Simulated waveforms were synthesized based on the expected value of a fluorescence signal using Poisson statistics. We synthesized 400 amplitude-modulated waveforms, each containing 8,000 samples for each set of input parameters, which included modulation frequencies between 30-39 MHz and average fluorescence intensities of 0.5, 1, 2, 4 photons per time sample. A sampling rate of 160 MHz was used in these simulations. Linear combinations of computer-generated waveforms were analyzed in MATLAB using the built-in FFT function to estimate amplitude or power spectra averages at a given frequency.

To compare the performance of TPFDMM and TPLSM methods, we calibrated large FOV TPLSM system [3] (MultiPhoton MesoScope, Thorlabs) to quantify calcium signals recorded in actual *in vivo* imaging experiments in photonic units. Fluorescence signals were detected using a photomultiplier (HC11706-40, Hamamatsu) coupled to a current amplifier (HCA-400M-5K-C, FEMTO) and a 50 MHz low-pass filter (Mini-Circuits). Waveforms showing single photon detection events were recorded with an oscilloscope (204MXi-A, LeCroy) at 1 GS/s rate without low-pass filtering. Spontaneous neuronal activity was

recorded in the Slc17a7-IRES2-Cre mouse, in compliance with the Allen Institute's animal imaging protocols.

3. Cross-talk analysis in frequency-multiplexed two-photon imaging.

Measurements of stochastic quantum events such as fluorescence emission are governed by Poisson statistics [18]. At a fixed excitation intensity, the recorded emission signals from a stable and uniform source sampled over discrete time intervals will vary randomly, a phenomenon is known as shot noise or Poisson noise, while the ensemble's variance and the mean will remain equal given sufficiently large sample size. When adding signal sources with independent, i.e. uncorrelated, noise components, the relationship between the ensemble mean and the variance remains, as each parameter is the sum of its respective components. For each excitation event at time t the detected emission signal $F(t)$ can be tentatively separated into the sum of an average or expected signal S_0 and purely random (stochastic) noise components $R(t)$. Considering multiple detection events, we may write the following set of equations:

$$F(t) = S_0 + R(t); \ \langle F(t) \rangle = S_0; \ \langle R(t) \rangle = 0, \ t \to \infty; \ S_0 = Var(R(t)) = \langle R(t)^2 \rangle \quad (1)$$

If the measurement events are ergodic and independent, which is the case for fluorescence signal detection, Eq. 1 can be applied to the scenario where the expected signal $S(t)$ varies periodically in time and only its average remains constant. For periodically modulated excitation intensity $I(t)$, the expected two-photon emission signal $S(t)$ is given as:

$$I(t) = I_0 \frac{\cos(2\pi ft) + 1}{2}; \ S(t) = A\left[1 + \frac{4}{3}\cos(2\pi ft) + \frac{1}{3}\cos(4\pi ft)\right]; \ A = \frac{3}{8}\sigma I_0^2, \quad (2)$$

where I_0 is the maximum excitation intensity, f is the modulation frequency, A s the average emission signal expressed here in units of photons/pulse, and σ is the proportionality coefficient connecting excitation intensity and emission signal in specific experimental conditions. Note that in the case of amplitude-modulated excitation, we expect to detect 3/8 of the total number of photons as compared to unmodulated excitation of the same average power. We may consider sub-ensembles of $F(t)$ that correspond to the same expected value $S(t)$ and recombine these sub-ensembles to obtain similar expression as in Eq. 1:

$$\langle S(t) \rangle = Var(R(t)) = \langle R(t)^2 \rangle \quad (3)$$

Noise variance is related to the power spectrum of a signal. For instance, in a case of discrete measurement of a time series signal, and in the specific case considering our noise component $R_i(t)$, Parseval's theorem states:

$$\sum_{i=0}^{N_s-1} |R_i(t)|^2 = \frac{1}{N_s} \sum_{k=0}^{N_s-1} |R_k(f)|^2 = \langle P \rangle, \quad (4)$$

where $R_k(f)$ is a discrete Fourier transform (DFT) complex variable corresponding to a frequency f, N_s is the number of recorded time samples, and $\langle P \rangle$ is the average of the noise power spectrum. On the left is the sum of the corresponding average values $\langle R(t)^2 \rangle$, and combining with Eq. 3 we obtain:

$$\langle S \rangle \cdot N_s = \langle P \rangle \quad (5)$$

In the case of multiple emission sources, provided they are statistically independent, Eq. 5 can be written as:

$$N_s \sum_{j=1}^{N_{ch}} \langle S_j \rangle = \sum_{j=1}^{N_{ch}} \langle P_j \rangle, \quad (6)$$

where N_{ch} represents the number of contributing signals or channels. Eqs. 5,6 provide the straightforward connection of a total average emission signal to the power spectrum average of a corresponding noise time series. To compute an average amplitude spectrum estimate we recall that DFT values, both real and imaginary, are a weighted sum of random noise variables. With a sufficient number of measurements, these values represent a normal 2D distribution in the complex space. One may derive probability distributions of $\left|R_k(f)\right|^2$ and $\left|R_k(f)\right|$ which originate from the same normal distribution and demonstrate that:

$$\left\langle \left|R_k(f)\right| \right\rangle = \sqrt{\frac{\pi}{4}\left\langle \left|R_k(f)\right|^2 \right\rangle} \tag{7}$$

The noiseless two-photon signal corresponding to a frequency f and peak-to-peak amplitude $\frac{3}{8}A$ (see Eq. 2) has DFT amplitude spectrum value:

$$\left\langle S(f) \right\rangle = \frac{2}{3}A \cdot N_s \tag{8}$$

Combining Eqs. 6-8 we obtain the signal-to-background ratio (SBR) estimate, which is a ratio of a DFT amplitude of a noiseless harmonic to the average background created by noise in all contributing signals:

$$SBR = \frac{4}{3}A\sqrt{\frac{N_s}{\pi \cdot \sum_{j=1}^{N_{ch}} A_j}} \tag{9}$$

We can see that the SBR increases as the square root of the number of measurements, and decreases as the square root of the sum of average emission intensities in each amplitude-modulated channel.

4. Numerical analysis of amplitude-modulated waveforms

To demonstrate validity of the analysis above, we performed numerical simulations of amplitude-modulated signals in the presence of shot noise and estimated signal and cross-talk values for a given number of samples and contributing channels. Figure 1a shows simulated waveforms from a single channel modulated at 30 MHz and a sum of 10 channels modulate at frequencies 30-39 MHz. The average amplitude of each waveform is 0.5 photons per sample.
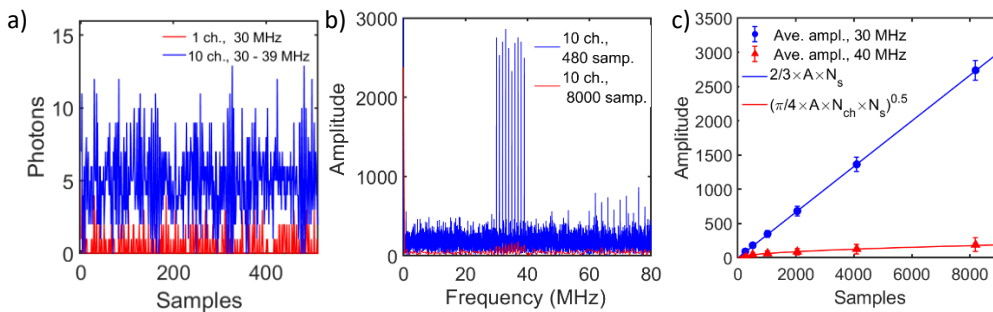

Fig. 1. (a) Computer-generated waveforms from 1 and 10 simultaneous channels amplitude-modulated at 30 MHz and 30 – 39 MHz. Average intensity in each channel is 0.5 photons/sample. (b) DFT spectra of the simulated waveform (blue trace in (a)) computed from 480 and 8000 time samples. (c) Average DFT amplitudes at 30 MHz and 40 MHz, representing signal and background from 10 active channels. The corresponding waveform example is shown in (a) in blue. Theoretical predictions via Eqs. 7,8 are shown as solid lines.

Fig. 1b shows Fourier spectra of 10 combined waveforms containing 480 and 8,000 samples. The contrast between the signals and the background is markedly enhanced with an increased

number of samples. Plotting the DFT signal $\left\langle \left| R_k(30MHz) \right| \right\rangle$ and background $\left\langle \left| R_k(40MHz) \right| \right\rangle$ amplitudes as a function of N_s computed from 400 simulated traces reveals the trends predicted by Eqs. 7,8 (Fig. 1c). Solid lines show theoretical predictions which are in excellent agreement with our simulation results. To illustrate adverse effects of cross-talk on the image quality and measurement accuracy of functional signals, we created images from 1 to 10 combined waveforms, whereas each pixel intensity corresponded to $R_k(f)$ values ($f = 30 - 40$ MHz) in the DFT spectrum normalized to the expected photon intensity per pulse. Only 160 time samples from each waveform with an average amplitude of 0.5 photon/sample were used in computing pixel intensity. Here waveform recording time per pixel was 1 μs, and the signal intensity was equivalent to 1 photon per laser pulse, assuming 80 MHz laser pulse rate. The images shown in Fig. 2a are arranged in a 10 × 10 matrix. Rows contain images from 1 to 10 active channels each modulated at different frequency, and the columns correspond to the specific modulation frequency. One can see the progressive increase of noise in the images and the appearance of background as the number of active channels increases. In our prior work [17], we discussed that frequency-multiplexed imaging performance in terms of SNR is similar to conventional TPLSM given the same data acquisition rate and the same number of photons generated by each excitation pulse. Fig. 2b shows simulated images from a conventional TPLSM that can be compared row by row to the images in Fig. 2a. As the number of channels in TPFDMM increases, the signal integration time in TLPSM is reduced proportionally. Pixel averages and corresponding standard deviations from images in Fig 2a, columns at 30 MHz and 40 MHz, and in Fig. 2b are presented in Fig. 2c. There is a clear quantitative similarity in SNR values of TPLSM and TPFDMM with the stated comparison criteria. Besides additional noise, each TPFDMM image will contain ghost images due to shot noise-induced cross-talk, which will increase proportionally to the square root of sum of average signal intensity in every channel. In Fig. 2d we replotted the TPFDMM data from Fig. 2c in units of DFT amplitude to demonstrate quantitative agreement with Eqs. 7,8.
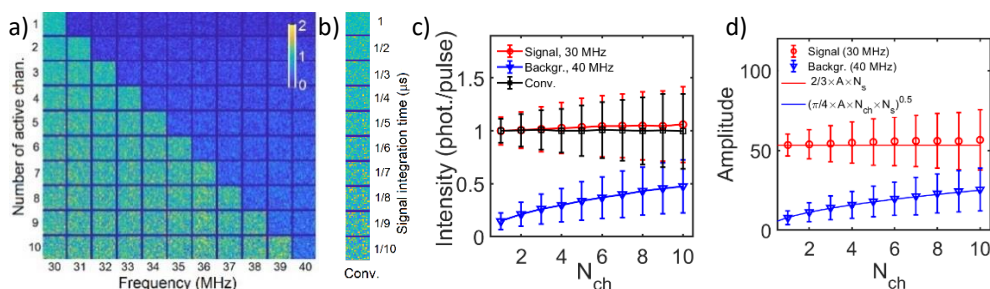

Fig. 2. (a) Simulated frequency-multiplexed images from 1 to 10 active channels. Pixel intensity is scaled to the average intensity expressed in photons/pulse. (b) Conventional TPLSM images generated with different pixel dwell times. (c) Average and standard deviation of pixel intensity values computed from images in (a) and (b) and expressed in units of photons per pulse. (d) A comparison of data from (c) plotted as DFT amplitudes and theoretical predictions from Eqs. 7,8.

5. Frequency-multiplexed imaging *in vitro*

We acquired images from brain slices containing neurons labeled with the calcium indicator GCaMP6f by scanning a single neuron with 3 beams modulated at 1, 5, 7 MHz (Fig. 3). For visualization purposes, the corresponding focal points in the image plane were laterally offset by ~ 20 μm each. A digitizer with data streaming capabilities allowed acquisition of complete waveforms corresponding to scan lines across an image. Each line contained 1,274,000 samples, which were binned into 1,000 time samples per pixel in post-processing. A conventional TPLSM image (Fig. 3a), computed from the waveform's average value, displays a triple image of the same neuron. Besides the main three, one can notice additional faint images of the same neuron resulting from additional weak excitation beams.

These extra beams appear due to the limited dynamic range of the radio-frequency (RF) amplifiers, specifically due to a non-linear amplifier response to the periodic spikes in the amplitude of an AOD RF driving signal created by the linear combination of three harmonics. These artifacts are not essential and will be ignored in the following discussion. Demultiplexed imaging corresponding to frequencies 7, 1, 5 MHz are presented in Fig. 3b, c, d, respectively. False color intensity scales in Fig. 3a and Fig. 3b-d are matched to allow visual comparison between conventional and frequency-encoded two-photon images. Demultiplexed images at a given frequency exhibit a single neuron along with two ghost images, which appear due to wideband shot noise in active signals modulated at different frequencies. This cross-talk will be reduced if we increase the number of samples and thus narrow the detection bandwidth. Fourier transform spectra also contain phase information, which we extract by computing the 4-quadrant inverse tangent of the imaginary to the real part ratio of the complex DFT value at a selected frequency. Figure 3e shows the computed phase values from each pixel/waveform within ROI corresponding to the cell body from Fig. 3a. It becomes evident that the phase within vertical scan line changes monotonically, and that the rate of phase change depends on the beam modulation frequency. Figure 3f,g shows wrapped and the corresponding unwrapped phase plots obtained from selected vertical lines across phase images in Fig. 3e. A linear fit of the lines in Fig. 3f yields the rates of phase change equal to -216, -163, -28 mrad/μs, corresponding to 7, 5, 1 MHz amplitude-modulated emission signals, respectively. Notably, the relative values of phase change rates do not quantitatively match the ratios between 7, 5, 1 MHz frequencies. The relationship of the phase within TPFDMM images and the signal modulation frequency is the subject of a future study. However, we note that the phase is determined by several factors, including the rate of an excitation beam movement across an image plane and phases of the AOD driving frequencies that create amplitude modulation in the excitation beams.
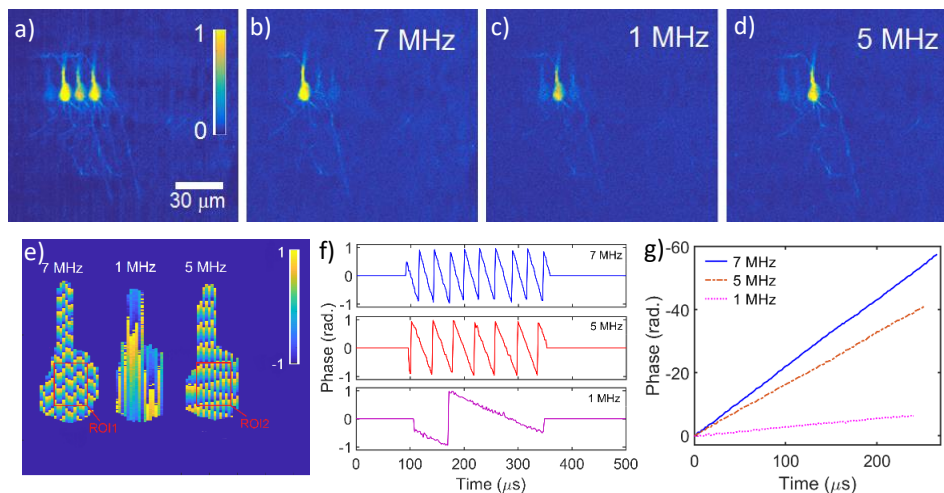

Fig. 3. (a) Conventional two-photon image of a brain tissue slice recorded while scanning a tissue sample with 3 excitation beams modulated at 7 MHz, 1 MHz, and 5 MHz. (b,c,d) Demultiplexed images corresponding to different frequencies. (e) Phase image from pixels within selected ROIs in (a) outlining a cell body. (f) Phase plots as a function of time obtained from selected vertical lines within phase images in (e). (g) Phase plots from (e) unwrapped and shifted to common origin.

As follows from Eq. 9, cross-talk between channels in TPFDMM can be reduced by binning the image into smaller number of pixels thereby sacrificing imaging resolution. One of the most essential applications of TPLSM is functional recording of fluorescence signal changes in Ca^{2+} indicators which are linked to neural activity. The signal is recorded from an area occupied by neuron soma that is more than 100× larger than the size of an individual pixel. To fully utilize advantages of the TPFDMM method, it is essential to treat the signals

acquired from a ROI as one continuous waveform which consists of individual parts corresponding to lines or pixels within. As we have demonstrated earlier (see Fig. 3), the phase of each pixel can be determined from the recorded trace itself. Other methods of tracking the phase which do not rely on the phase calculation from noisy signals may be developed as well, for example, by independently recording phases of both the excitation beams and the optical scanner. Once phase information is available, it is trivial to align the phases of each individual component and reconstruct an extended waveform.

As a demonstration, we selected identical ROI1 and ROI2 with the same number of pixels from neuron images in Fig. 3 corresponding to 5 MHz and 7 MHz excitation beams (see Fig. 3e). We examined contributions of the main signal modulated at a given frequency to the other frequency channel after performing phase-alignment and reconstruction of extended waveforms based on known phase information. Specifically, we performed identical phase adjustments of waveforms/pixels within ROI1 and ROI2 using the measured phase in either the 7 MHz or the 5 MHz channel, and compared spectral amplitudes at these frequencies. Each pixel therein consists of 1,000 samples, which contains exactly 14 and 10 periods of 7 MHz and 5 MHz frequencies sampled at 500 MHz. Phases of each waveform were adjusted to 0 phase difference by cyclic rotation of samples within (MATLAB's *circshift* function). Due to waveform discretization, phase adjustments can be performed within a finite accuracy of 63 and 88 mrad for 5 and 7 MHz frequencies, respectively. Note that phase adjustment precision may be improved, for example, with interpolation and digital oversampling. Next, arrays were concatenated to form phase-aligned waveforms, whose DFT spectra are shown in Fig. 4. To avoid ambiguity, we explicitly denote DFT spectra R_{11} and R_{12} computed from ROI1 and ROI2 waveforms, respectively, aligned using 7 MHz / ROI1 phase information. DFT spectra R_{22} and R_{21} were obtained from ROI2 and ROI1, respectively, aligned using 5 MHz / ROI2 phase information. R_{11} primarily contains a signal modulated at 7 MHz, and the frequency domain amplitude of this component is the only one clearly visible in the spectrum (Fig. 4a top, blue line). R_{12} contains 5 MHz signal, which is also seen in the frequency spectrum in the same panel, albeit with signal spread over neighboring frequency bins due to dephasing. Notably, cross-talk $R_{12}(7MHz)$ becomes negligible. A similar outcome is seen in the bottom panels of Fig. 4a,b where phase information from 5MHz emission signal was used for waveform alignment.
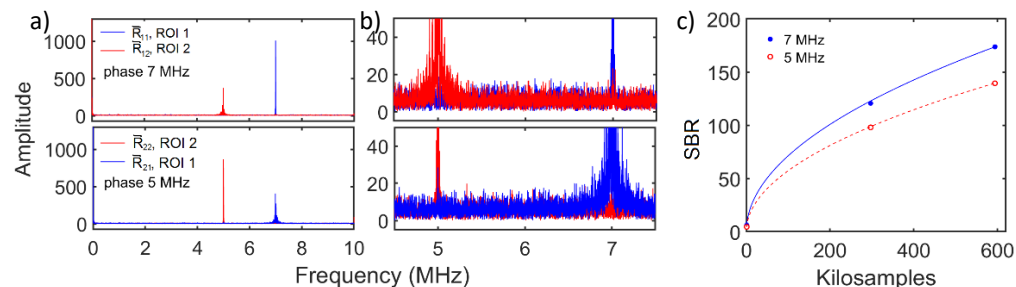

Fig. 4. (a) Frequency spectra of phase-aligned and concatenated waveforms from pixels within ROI1 and ROI2 shown in Fig. 3e. Waveform phase alignment in upper and lower tiles was performed with phase values 7 MHz and 5 MHz in Fig. 3e, respectively. (b) Data in (a) shown with expanded X and Y scales to demonstrate residual crosstalk. (c) SBR dependence on the number of samples in phase-aligned datasets. Fits $\sim \sqrt{N_s}$ are shown as solid lines.

Using the data from Fig. 4a, we computed the SBR as $R_{11}(7MHz)/R_{12}(7MHz)$ and $R_{22}(5MHz)/R_{21}(5MHz)$. Similar comparisons can be made with datasets with reduced

number of samples. Fig. 4c shows SBR as function of N_s, demonstrating the expected square root of N_s dependence.

6. TPLSM photon collection efficiency *in vivo*

Signal intensity is another critical parameter affecting cross-talk between frequency channels. To establish a connection with theoretical estimates we must quantify the number of photons detected in real experiments. One approach is to measure the system conversion gain g using mean-variance or photon transfer curve method [19]. Although it is considered applicable to CCD and CMOS sensors, the method needs adaptation for amplified detectors due to the presence of additional noise sources which increase the signal variance [20]. To perform these measurements another system was used, the Multiphoton MesoScope [3], because of its highly optimized collection efficiency. To quantify g we used a direct correlation of the average number of photons from a stable emission source measured with photon counting technique and the average pixel intensity in the TPLSM images. In this experiment, waveforms showing individual photons and the corresponding images of a fluorescein solution were acquired at different excitation power levels. Waveforms examples are presented in Fig. 5a. Only spikes with an amplitude exceeding 40 mW were counted as photon detection events. Fig. 5b shows variations in the number of photons detected within a temporal window of 10 µs and Fig. 5c shows the corresponding mean-variance plot. We observed small deviation of ~ 15-20% from the expected trend, which may be caused by variations in the average photon flux as the beam moves across an imaging plane. Image non-uniformities in the range of ~ 10% are seen in averaged TPLSM images recorded from fluorescein solution, and were reported previously [3]. They do not significantly affect conversion gain measurements.
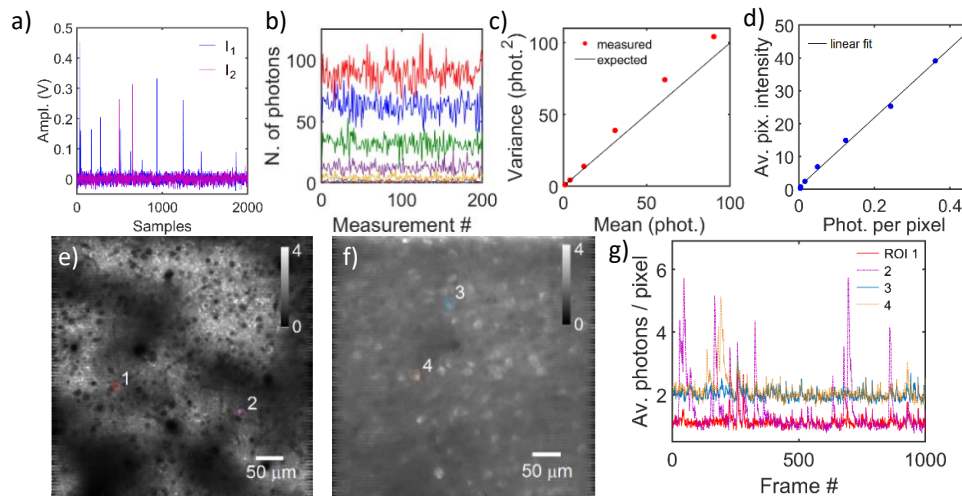

Fig. 5. (a) Examples of photomultiplier output showing individual photons at different fluorescence signal intensities. (b) Fluctuations in the detected number of photons within 10 µs temporal window recorded at different excitation power levels. (c) Mean - variance plot of signals from (b). (d). Calibration plot showing average pixel intensity in TPLSM images as a function of average number of detected photons. (e,f) Averaged *in vivo* images of V1 layer 1 and 4 of a mouse recorded at depths 75 µm and 375 µm. Intensity scale is in units of photons per pixel. (f) Examples of calcium signal transients from selected ROIs.

In the central part of the scan line that contains 512 pixels, a 12 kHz resonant scanner moves with the highest speed, and the pixel dwell time is ~ 40 ns. The correspondence between average pixel intensity in the central part of the image and the average number of photons scaled proportionally to the pixel dwell time is shown in Fig. 5d. Linear fit yielded conversion

gain g $\approx$ 106 phot.$^{-1}$·pixel^{-1}. We note that straightforward application of the mean-variance method without corrections yielded noticeably smaller g $\approx$ 44 phot.$^{-1}$·pixel^{-1}.

In vivo images of spontaneous activity within a mouse visual cortex recorded at depths of 75 µm and 375 µm, averaged 1000 times and scaled to show image intensity in photonic units detected, are shown in Fig. 5e,f. Extracted Ca^{2+}-traces from selected cells scaled in units of average photons per pixel within the selected regions of interest are shown in Fig. 4g. Each pixel integrates signals from 3-4 excitation pulses, and the observed fluorescence signals from selected cells vary in the range $\sim$ 0.1 – 2 photons per pulse. Background signals fluctuations resulting from out of focus fluorescence appear at the level ~0.1 photons per pulse (2 standard deviations) and define the sensitivity threshold of detecting a calcium signals from individual neurons. Note that photon intensities assumed in numerical simulations match the range observed in the experiment. Knowing these signal levels, Eqs. 7-9 can be directly used to evaluate cross-talk between frequency channels in TPFDMM when fluorescence is detected with photon counting methods.

7. Discussion

The major benefit of TPFDMM is its ability to utilize a significantly higher number of imaging channels [15, 21] as compared to alternative multiplexed imaging methods and to potentially achieve major increases in imaging throughput as well as the rate of volumetric recording of functional brain activity. Unlike time-multiplexed approaches [12, 13, 16], TPFDMM is not limited by the fluorescence lifetime of an optical indicator and can utilize multiple laser sources without pulse synchronization between excitation channels. While our approach achieves high modulation frequencies which are needed to support high scanning speed, the maximum usable modulation frequency is ultimately limited by the laser pulse repetition rate and the pixel dwell time. To be able to separate individual frequency components, pixel dwell times must accommodate at least one and preferably several periods of each modulation frequency. For example, TPLSM with 512 pixels per scan line has a minimum pixel dwell time in the range of 40-120 ns, depending on the speed of the RG scanner, which corresponds to 3-10 excitation pulses per pixel at 80 MHz laser repetition rate. Clearly, only the slowest 4 kHz RG mirror may potentially support frequency-multiplexed imaging with a few channels. TPFDMM performance can be substantially improved by increasing the laser repetition rate and thus the range of available modulation frequencies as well as increasing pixel dwell time and binning the image into a smaller number of pixels. Earlier, we discussed that TPFDMM matches the performance of TPLSM in terms of imaging resolution and SNR at the same fluorescence signal intensity per channel and the same data acquisition rates (see Fig. 2a-c, and [17]). This comparison assumes that the signals of equal intensity are present in every channel, which clearly is not the case in real experiments. When imaging multiple ROIs sequentially with the TPLSM, a significant delay is needed to reposition the scanning beam. For example, the Multiphoton Mesoscope achieves the transition time of ~10 ms, which is comparable to a 23 ms single frame acquisition time [3]. This dead time may be either eliminated or at least reduced proportionally to the number of channels in TPFDMM. When combined, these benefits can significantly improve TPFDMM performance.

Additional benefits of TPFDMM become apparent when we consider specific applications such as the functional recording of calcium signals from neurons. In this work, we demonstrated that cross-talk and noise contributions from other frequency-encoded channels can be reduced proportionally to the square root of the acquisition time needed to measure a signal from every pixel within a cell body. For example, the signal acquisition time equals ~7 µs, given single cell body ~15 µm in diameter and a dwell time of ~40 ns/µm when using the fastest 12 kHz RG scanner. Assuming average signal intensities of 0.5 photons per pulse in each imaging channel, the resulting SBR is approximately 9 and 6, for 2 and 4 imaging channels, respectively (see Eq. 9). Therefore, we may expect to see noise at the level

of ~0.05 – 0.08 photons/pulse when imaging with 2 – 4 channels simultaneously. In the example shown above, the background noise of calcium signals appears at the similar level in the range of ~0.1 photons per pulse. Note that these measurements were performed with analog and not photon counting detection, and therefore noise levels are slightly overestimated in this comparison. It is possible to conclude that at these fluorescence signal intensities (~0.5 photon/pulse) and scan speeds (40 ns/µm), TPFDMM will allow reliable detection of Ca^{2+} spikes from multiple simultaneously-imaged channels. Using slower scan speeds provided by 8 and 4 kHz RG scanners will only improve TPFDMM performance.

A major limitation for TPFDMM which also affects every other TPLMS imaging method is the physiologically acceptable excitation power levels for *in vivo* applications. Prior studies have placed this limit at ~250 mW with ~900 nm excitation [22]. We mentioned previously that amplitude-modulated excitation is expected to generate 3/8 of the average signal as compared to conventional unmodulated excitation (Eq. 2). To compensate for the signal loss, input power must be increased by $\sqrt{8/3}$ for two-photon imaging. Clearly, if multiple beam foci are distributed in the same imaging plane, the input power will increase proportionally to the number of excitation beams. Since the required power increases exponentially with depth, it appears advantageous to position the beams with an axial offset and distribute laser power unevenly between scanning beams. It is possible, however, to greatly reduce the overall exposure by restricting image acquisition to the selected ROIs which include, for example, only cell bodies and exclude empty spaces that do not contain useful information [23].

8. Conclusions

In this work a utility of TPFDMM method for functional *in vivo* recordings of calcium signals was studied. Analytical expressions were derived, describing the relationship between average two-photon emission intensity in each channel and expected cross-talk arising due to shot noise in other active channels, and the results were verified with numerical simulations. We proposed a novel approach that leverages phase information within individual pixels in the selected ROI to synthetically extend waveform measurement time and thus significantly reduce cross-talk between active channels. Practical application of this method was demonstrated *in vitro* by imaging GCaMP6f-labeled slices of brain tissue with multiple frequency-encoded beams. We also established a quantitative relationship between the signal intensities detected during *in vivo* experiments and theoretical predictions to guide TPFDMM performance evaluations. Our results suggest that *in vivo* calcium signal levels detected in real *in vivo* experiments are sufficient for TPFDMM. Novel calcium indicators such as GCaMP7 [24] with increased fluorescence efficiency may further improve the performance of this imaging method. While we examined only one specific use case of TPFDMM, other applications of this method are feasible. For example, spatially-multiplexed TPLSM with multiple excitation beams and multiple detectors [25] or random access scanning [9] may incorporate frequency-encoded excitation and detection to improve data acquisition rates and the quality of information recorded. We note that the TPFDMM method is technically complex and still under development. Flexible positioning of excitation beams within FOV, management of significantly higher data streams as compared to conventional TPLSM, real-time image reconstruction methods, as well as new image segmentation and postprocessing algorithms are needed to bring TPFDMM into the realm of practical applications.

9. Acknowledgements